Tunneling explains efficient electron transport via protein junctions

Jerry A. Fereiro[a], Xi Yu[a,1,2], Israel Pecht[b,1], Mordechai Sheves[c,1], Juan Carlos Cuevas[d,e,1], and David Cahen[a,1]

[a]Department of Materials and Interfaces, Weizmann Institute of Science, Rehovot 7610001, Israel; [b]Department of Immunology, Weizmann Institute of Science, Rehovot 7610001, Israel; [c]Department of Organic Chemistry, Weizmann Institute of Science, Rehovot 7610001, Israel; [d]Departamento de Física Teórica de la Materia Condensada, Universidad Autónoma de Madrid, 28049 Madrid, Spain; and [e]Condensed Matter Physics Center (IFIMAC), Universidad Autónoma de Madrid, 28049 Madrid, Spain

Edited by Harry B. Gray, California Institute of Technology, Pasadena, CA, and approved April 9, 2018 (received for review November 15, 2017)

Metalloproteins, proteins containing a transition metal ion cofactor, are electron transfer agents that perform key functions in cells. Inspired by this fact, electron transport across these proteins has been widely studied in solid-state settings, triggering the interest in examining potential use of proteins as building blocks in bioelectronic devices. Here, we report results of low-temperature (10 K) electron transport measurements via monolayer junctions based on the blue copper protein azurin (Az), which strongly suggest quantum tunneling of electrons as the dominant charge transport mechanism. Specifically, we show that, weakening the protein–electrode coupling by introducing a spacer, one can switch the electron transport from off-resonant to resonant tunneling. This is a consequence of reducing the electrode's perturbation of the Cu(II)-localized electronic state, a pattern that has not been observed before in protein-based junctions. Moreover, we identify vibronic features of the Cu(II) coordination sphere in transport characteristics that show directly the active role of the metal ion in resonance tunneling. Our results illustrate how quantum mechanical effects may dominate electron transport via protein-based junctions.

bioelectronics | resonance tunneling | protein junctions | temperature dependence | protein IETS

Proteins play a vital role in biological energy conversion processes, notably electron transfer (ET), such as in photosynthesis, respiration, and a wide range of enzymatic reactions (1, 2). Over the past decades, redox proteins with transition metal ion centers with variable valence were integrated into solid-state electronic junctions for electron transport (ETp) measurements (3–6). Apart from the fundamental interest in understanding solid-state ETp properties of proteins, their integration into hybrid junctions might lead to devices with designed electronic functions, a holy grail of bioelectronics (7, 8). Previous studies of the blue copper protein azurin (Az) containing junctions, with single, several (9–11), or multiple protein molecules (12), have suggested that the efficiency of their ETp is comparable with that via conjugated organic molecules as judged from the observed current densities at low bias (100 mV) (4). The presence of Cu was shown to increase the efficiency of transport across Az (13), with clear differences between its two oxidation states, Cu(I) or Cu(II) (14), involved in Az redox activity. ETp was found to be temperature independent (12), as observed also in other proteins (5, 6, 15–17), which can be interpreted as resulting from off-resonance tunneling, a view supported by inelastic electron tunneling spectroscopy (IETS) results (18).

ETp via redox proteins is characterized not only by the nature of the proteins in the junction but also, by protein–electrode interactions (19), the nature of the redox center (13), and their orientation relative to the electrode (6, 20) as well as proteins' structure (4, 13). Although there is no consensus on how exactly these parameters affect the ETp, it is generally agreed that protein–electrode coupling (16) plays a major role as in ETp via nonbiological molecules (21). Previous reports from our group and others have shown that, by varying the interaction between the redox site and the electrode (14, 16), both charge transport efficiency and its mechanism can be varied. For example, a Cytochrome C mutant having its heme close to the electrode exhibits less temperature dependence and higher conductance at low temperature (30–400 K) than that with the heme distal from the electrode (19), indicating that heme–electrode separation affects the charge transport. However, a detailed understanding of the role of electrode coupling to the proteins, especially with the redox site of ET proteins, still needs to be further investigated.

Here, we report results of a systematic low-temperature current–voltage (I-V) study of the mechanism of ETp across Az junctions by incorporating a spacing layer (linker) between Az and the electrode to alter redox site–electrode coupling. The I-V characteristics determined using two different junction configurations, Au-Az-Au (Fig. 1) and Au-Az/linker-Au (Fig. 2*C*, *Inset*), at low temperatures (10 K) show a dramatic change from the nearly linear shape observed without the linker to a step-like behavior in the presence of the insulating linker. As discussed below, these results together with the temperature dependence of the differential conductance and the vibronic signatures of the Cu(II) coordination sphere in the I-Vs provide strong evidence that ETp via these junctions is dominated by resonant tunneling. Specifically, we show that the step-like I-V patterns via the junctions observed in the presence of the linker are a signature of

Significance

Investigation of the charge transport mechanism across a monolayer of a redox active protein is important for the fundamental understanding of the naturally occurring electron transfer processes, such as those in photosynthesis or respiration. Inelastic electron tunneling spectroscopy measurements of a redox active protein may provide direct experimental evidence that the tunneling charges are, in fact, passing through the protein molecules. Results of our study of conductance via well-controlled azurin monolayer solid-state junctions show the direct involvement of the Cu(II) site in assisting electron transport, underscoring this site's vibronic characteristics associated with the charge transport mechanism. Our study widens the scope of currently available methodologies and also adds to the potential of using proteins in bioelectronics.

Author contributions: J.A.F., X.Y., I.P., M.S., and D.C. designed research; J.A.F., X.Y., and J.C.C. performed research; J.A.F., X.Y., I.P., M.S., J.C.C., and D.C. analyzed data; and J.A.F., X.Y., I.P., M.S., J.C.C., and D.C. wrote the paper.

The authors declare no conflict of interest.

This article is a PNAS Direct Submission.

[1]To whom correspondence may be addressed. Email: xi.yu@tju.edu.cn, Israel.pecht@weizmann.ac.il, mudi.sheves@weizmann.ac.il, juancarlos.cuevas@uam.es, or david.cahen@weizmann.ac.il.

[2]Present address: Department of Chemistry, Tianjin Key Laboratory of Molecular Optoelectronic Science, Tianjin University, 300072 Tianjin, China.

This article contains supporting information online at www.pnas.org/lookup/suppl/doi:10.1073/pnas.1719867115/-/DCSupplemental.

Published online April 30, 2018.

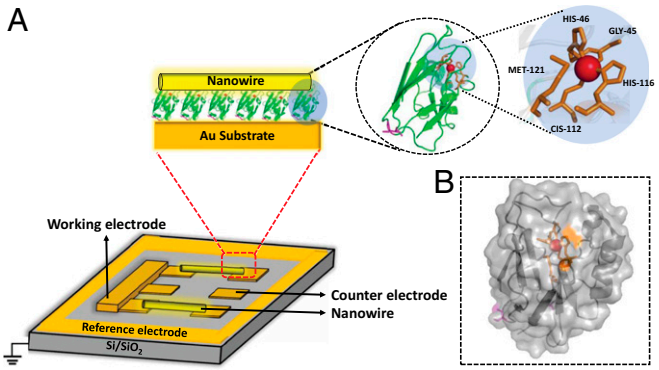

Fig. 1. (*A*) Schematic illustration of the solid-state protein junction prepared by trapping nanowires to produce contacts for electrical transport measurements. *Left Inset* shows the structure of Az (Protein Data Bank ID code 1azu), where violet denotes the disulfide bridge of the two cysteine residues and red denotes the Cu redox center along with its coordination sphere given in orange (enlarged in *Right Inset*). *B* shows a semitransparent view of the surface of Az indicating the imidazole residue of His-116, which is part of the Cu(II) coordination sphere (as shown also in *A*, *Right Inset*), exposed on the surface (shown in orange).

coherent resonant tunneling involving the Cu(II) ion, a phenomenon never reported before for protein junctions.

Junction Fabrication

Fig. 1 shows the schematic structure of the Au-Az-Au suspended nanowire junction that was used in these experiments. This configuration was found to be stable over a wide temperature range, which allows I-V measurements and the collection of results of the voltage dependence of dI/dV (conductance) and d^2I/dV^2 (IETS) (22). Significantly, the latter probes the interaction of the electronic current with the vibrational modes of the molecules in the junction (22, 23).

Micrometer-sized Au electrodes were fabricated on an Si wafer by photolithography, and full details of junction fabrication and monolayer formation are reported in *SI Appendix*. Monolayer characterization using atomic force microscopy (AFM) established that the proteins are densely packed, with no aggregates over 25-μm^2 areas (i.e., orders of magnitude larger than the area between the contact and the Au nanowire). The protein monolayers were further characterized by ultraviolet-visible spectroscopy and polarization–modulation infrared reflection–absorption spectroscopy (*SI Appendix*, Figs. S2 and S5).

After characterization, the protein monolayers were contacted with the Au nanowires using dielectrophoresis (24, 25), where individual Au nanowires are electrostatically trapped between two microelectrodes forming top electrodes, thereby producing a junction between the Az monolayer on the lithographically prepared Au electrodes and the electrostatically trapped single Au nanowire (Fig. 1). The geometric junction area (26) was estimated to be ~5,000 nm^2 (i.e., formally up to maximally 2,000 Az molecules could be involved in the junction).

For investigating the impact of adding a linker onto one electrode, the Au nanowires (top gold electrodes) were first modified with a monolayer of linker molecules by incubating Au nanowires in either a mercaptopropionic acid (MPA) or a mercaptohexanoic acid (MHA) solution (*SI Appendix*) before trapping them dielectrophoretically to obtain the Au-Az/MPA-Au (Fig. 2*C*) or Au-Az/MHA-Au configurations.

Experimental Comparison Between Two Configurations

In our experiments, the I-V, dI/dV (conductance), and d^2I/dV^2 (IETS) were obtained by simultaneously using direct source–meter measurements and lock-in amplifier. The I-V curves, obtained for Au-Az-Au junctions (i.e., bare gold electrodes) at low temperature (10 K), are linear (red line in Fig. 2*A*). The conductance curve was temperature independent (10–300 K) as we have reported previously (18). The small kinks observed in the conductance spectrum (dI/dV vs. V) (Fig. 2*A*, black line) indicate the opening of inelastic conduction channels at voltages corresponding to energies of vibrational modes, while the dip near zero bias is attributed to the large number of low-energy vibrations (27). The IETS peak around 3,000 cm^{-1} (Fig. 2*B*) corresponds to the C-H stretching mode, and those at 1,640/1,520 cm^{-1} correspond to the Amide I and Amide II bands, respectively. Furthermore, as we have shown earlier, the line shape obtained for the IETS spectra indicates the operation of an off-resonance mechanism for the inelastic transport (18).

Fig. 2 *C* and *D* shows the results obtained using the Au-Az/(linker)-Au configuration, where the gold nanowire was modified with a monolayer of MPA to reduce electrode/protein coupling at one of the contacts. [Two different linkers, MPA and MHA, were tested to show the reproducibility and reliability of the experiment. The results obtained with the MHA linker are given in *SI Appendix* (*SI Appendix*, Figs. S8 and S9).] In this configuration [Au-Az/(linker)-Au], the I-V characteristic at 10 K exhibit steps, and the conductance vs. applied voltage curve shows a clear peak structure (Fig. 2*C*), suggesting that charge transport is mediated through discrete energy levels in the protein that are accessible within the applied bias window. Fig. 2*D* shows the d^2I/dV^2 results obtained from the [Au-Az/(linker)-Au] junction, which can be compared with those obtained without the linker (Au-Az-Au) (Fig. 2*B*). The observed dI/dV–V behavior of the [Au-Az/(linker)-Au] junction may be interpreted by either a change in tunneling regime from off-resonant to resonant or the occurrence of Coulomb blockade (21, 28–30). As we show below, our analysis of the temperature dependence of the transport properties favors the former interpretation, and thus, in what

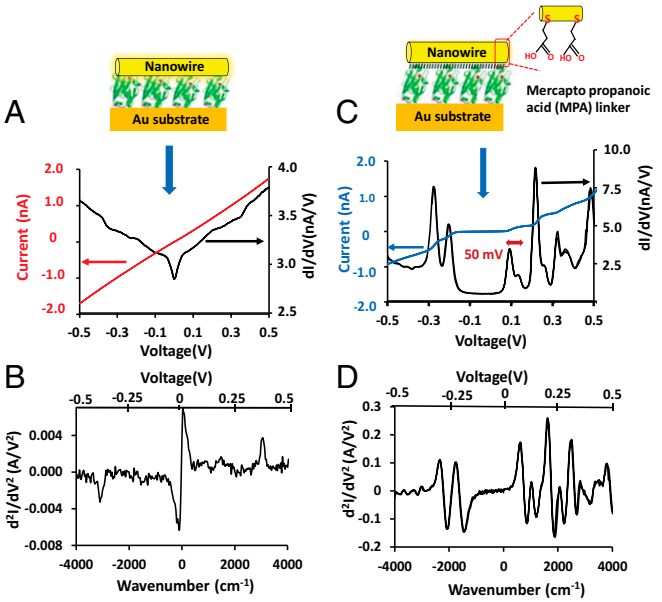

Fig. 2. (*A*) I-V (red) and conductance voltage (dI/dV–V; black) plots of the Az junction between −0.5 and +0.5 V. (*B*) IETS (d^2I/dV^2–V) of the same junction. (*C*) I-V plots (blue) of Az with (MPA) linker and conductance (dI/dV–V; black). (*D*) IETS (d^2I/dV^2–V) of the same junction with MPA linker. All data are for experiments at 10 K. The wavenumber 1/λ (centimeters^{-1}), where λ is the wavelength of the radiation (centimeters), is related to the applied bias, V, by E = qV = hc/λ (q is the electron charge, h is Planck's constant, and c is the speed of light), where E is the energy of the vibration mode.

follows, we shall interpret our data in terms of resonant tunneling (*SI Appendix*).

The results obtained using MPA-modified Au electrodes [Au-Az/(linker)-Au] (shown in Fig. 2*C*) are stable (as evidenced by being able to cycle the voltage without any change of features) and reproducible over time (*SI Appendix*). No significant charge transport occurs at low bias (Fig. 2*C*), which we interpret as the absence of significant electrode–protein energy-level overlap. We stress that the I-V plot near zero bias in Fig. 2*C* is linear. As this is difficult to see in Fig. 2*C* because of the low current due to the weak coupling, a magnified view of the I-V plot near zero bias is shown in *SI Appendix*, Fig. S15. Clear evidence for the linear behavior can be seen in the constant nonzero differential conductance (black solid line in Fig. 2*C*) close to zero bias. On raising the bias beyond the threshold, the current rises sharply, which suggests that a protein's energy level is brought into resonance with the chemical potential of one of the electrodes. The consequence is a step-like increase of the current with voltage or correspondingly, a peak in the differential conductance, dI/dV. As we shall suggest below, the relevant energy levels giving rise to these current steps most likely involve the Cu(II) coordination sphere of Az. While this type of step-like I-Vs has been reported in the context of single-molecule measurements in the weak and intermediate coupling regimes (31–34), it is observed here in protein-based junctions as a result of modulating redox site–electrode interactions.

We propose that the observed difference in conduction behavior of the Az junction in the presence and absence of the linker layer is due to the different coupling between the Cu(II) coordination sphere in Az and the top Au electrode surface. It is well-known in the context of molecular electronics that the degree of coupling to the leads determines not only the broadening but also, the position of the molecular energy levels (21). Fig. 1*B* shows that the Cu coordination sphere (of N and S atoms from surrounding amino acids) is partially exposed on the protein surface. Therefore, in the absence of a linker as a spacer between the protein and the electrode, the Cu(II) coordination sphere is practically in contact with the Au nanowire electrode, increasing the probability of wave function overlap between its orbitals and the latter electrode. We suggest that this strong coupling between the protein and the nanowire results in the broadening of relevant energy levels (closest to the E_F of the electrodes) of Cu(II), including its coordination shell. The linear I-V plots shown in red in Fig. 2*A* are consistent with the charge transport taking place through the tails of those energy levels that are outside of the transport window defined by the bias (see Fig. 6 and *SI Appendix*). Such a scenario for charge transport is also consistent with our finding that the I-V plots in this case are temperature independent (18). Similar behavior has been observed in other molecular systems (28, 35). In contrast, when the Cu(II) coordination sphere is shielded from direct interaction with the Au nanowire electrode by the linker molecule (MPA), the I-V curve shows current steps (Fig. 2*C*). The linker, in addition to the effect of its length, also conducts poorly, as it is a saturated hydrocarbon. In this weaker coupling situation, the electronic structure at the interface can be interpreted based on the native electronic state of the Cu(II) center and the Au wire electrode. The redox potential of the Cu(II) center of Az is around 4.75 eV vs. vacuum (36), which is close to the work function that we measured for the gold substrate modified with MPA. Thus, the relevant energy levels are now accessible for resonant transport with a moderate bias. It is important to note that the proteins are coupled asymmetrically in the Au-Az/linker-Au configuration via the linker to one electrode and by a direct Au-S bond to the other, creating an asymmetric voltage drop at the protein interfaces.

Examining Stability and Reproducibility

The stability and reproducibility of these results were established by using several different Az samples and on several different junctions prepared from each sample (Fig. 3). Fig. 3 shows the dI/dV results obtained using three different junctions (using three different protein samples, measurements were carried out on different days with identical experimental procedure) at 10 K. They all show that the peak-like behavior in the differential conductance plots is reproducible. While the position of the peak in the exact bias voltages varied, such peak structures were seen in 24 (~65%) of the 36 junctions that gave reliable measurements of 121 junctions. Approximately 35% (42) of 121 junctions were too unstable to measure in our probe station at low temperatures and shorted during the measurement, which takes ~2 h on each junction; for ~20% (24), contact was lost during the measurement, resulting in only background current (<3 pA). The remaining 19 junctions gave already from the start high currents (more than 10 nA at 0.5 V) and were not considered further. For the 24 junctions that gave peak structures, in most cases, clear, well-separated peaks were seen in the conductance (*SI Appendix*, Fig. S7 shows the statistics on peak position and for the number of peaks observed within the given bias range).

The observation of conductance peaks for different samples at different voltages (Figs. 2*C* and 3) and with varying intensities likely reflects differences in the electrostatic landscape. Hence, the exact peak shape depends on the electronic structure of the protein, the protein–electrode interactions (Au-protein/linker-Au junctions), and the orientation of proteins with respect to each of the electrodes as already observed previously for molecular junctions (37, 38). Slight changes in orientation of proteins can translate into significant changes in distance and electrostatic potential between the active centers and the gold, resulting in different interaction between its Cu(II) coordination sphere and the contacted linker molecule(s). Similar shifts in conductance peak with varying peak position and peak amplitudes have been observed using scanning tunneling microscopy (STM) measurements via C60 molecules (39, 40), indicating the importance of the conducting molecule's spatial location within the junction.

The actual number of molecules that are responsible for the measured ETp via a monolayer will be much smaller than that estimated from the geometric area (41). It depends on many parameters, including the roughness of both the substrate and the top contact, the density of proteins in the monolayer, and again, their orientation relative to the electrodes. This, in turn,

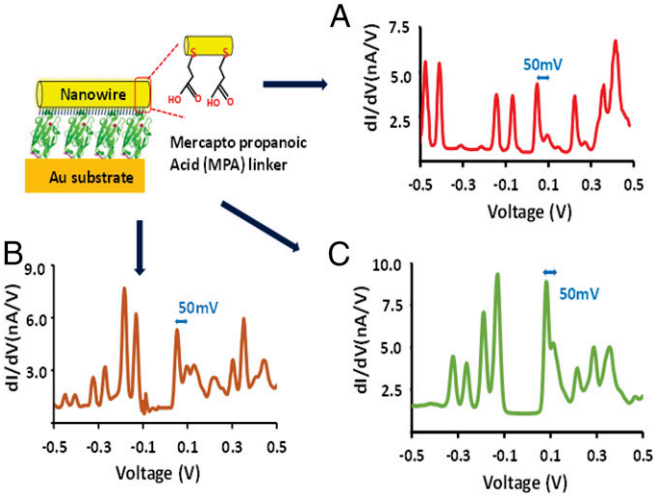

Fig. 3. (*A–C*) dI/dV vs. V plots of Au-Az/MPA-Au junction at 10 K carried out on different batches on different days.

will depend on how the proteins are bound to the Au surface (especially their orientation, as this can affect the roughness and the asperities in the monolayer) and how far adsorption of one protein affects that of others. For junctions with a geometric area of hundreds of micrometers squared, it has been estimated that only approximately ≤0.1% of the molecules dominate the transport process (42). This, for our junctions, would mean involvement of a few dozen Azs. In *SI Appendix* (*SI Appendix*, Table S2), we compare the current magnitudes that we measured with those of other reported Az (both single and monolayer) junction measurements, indicating that, in the junctions reported here, we measure the charge transport process through only a few proteins.

The significant difference observed in I-V characteristics of the protein junction caused by introducing the linker at the protein–electrode interface (Fig. 2 *A* and *C*) reveals the key role of protein–electrode coupling in ETp. Considering the similarity in the quantum tunneling nature between ET rates and electronic conductance [the analog being donor (acceptor)–protein coupling in ET], different models comparing them have been mentioned (43–46). Recent research has underlined the complex relation between them in molecular organic and biomolecular systems (47) and the differences between them (48) (*SI Appendix* has additional detailed discussion).

Role of Copper(II) Ions

To establish the involvement of the Cu(II) ions in the observed conductance behavior, we prepared junctions with Az depleted of its Cu ions (Apo-Az) (compare with *SI Appendix*). The optical absorption data (*SI Appendix*) show that the characteristic 625-nm absorption band associated with Cu(II) disappears in the Apo-Az. Fig. 4*A* shows the I-V and conductance results obtained with Au-(Apo-Az)/MPA-Au junctions. No steps are observed in the I-V, and no peaks of the conductance plots are seen (Fig. 4*A*, black), indicating that, without the metal ion, transport is again by off-resonance tunneling. In addition, the IETS spectra of Au-(Apo-Az)/linker-Au (Fig. 4*B*) junctions resemble those obtained for Au-Az-Au (Fig. 2*B*) junctions, with the C-H stretching peak at around 3,000 cm^{-1} and the peaks at 1,640/1,520 cm^{-1} that correspond to the amide bands (Fig. 3*B*).

We note that the current observed for Apo-Az is similar to that of Az (with linker). This seems odd, since transport across Apo-Az is off-resonance, which is supposed to be less conducting than resonance tunneling through Az (with linker). We account for this by the different tunneling distances in Az and Apo-Az. The monolayer thicknesses of Apo-Az and Az are 2.6 and 1.8 nm, respectively, as confirmed by ellipsometry and AFM. The exponential dependence of the tunneling current with respect to

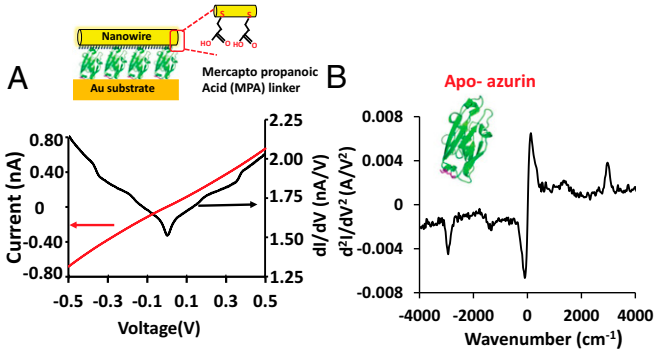

Fig. 4. (*A*) I-V (red) and conductance voltage (black) plots of the Apo-Az junction with MPA linker between −0.5 and +0.5 V. (*B*) IETS spectrum of the same junction, where IETS is shown as d^2I/dV^2 vs. V.

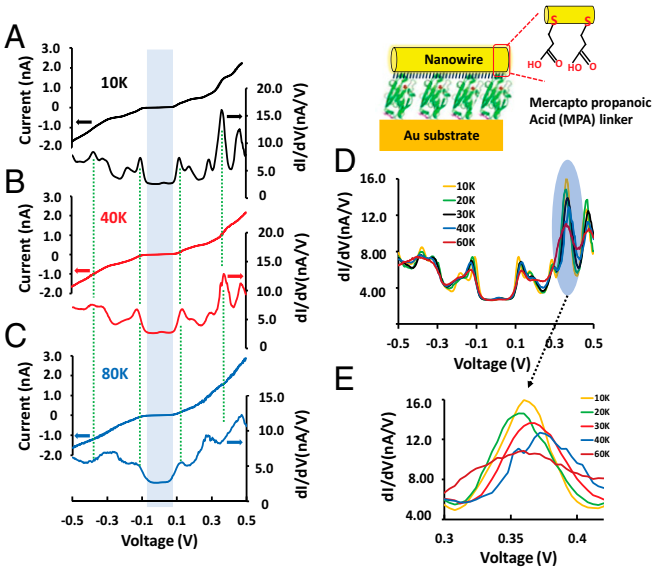

Fig. 5. *A–C* show the temperature dependence of the I-V and conductance (dI/dV) plots via the Au-Az/MPA-Au junctions (10, 40, and 80 K, respectively). *D* shows the conductance curves at different temperatures ranging from 10 to 60 K. *E* shows a zoomed in view of one of the conductance peaks from *D* at different temperatures.

thickness amounts to a decrease in current of 20–100 times for Az (assuming distance decay coefficients of 0.6–1.0/Å) (4) compared with that of Apo-Az. Therefore, this difference in tunneling distance (~0.8-nm difference) along with the additional thickness of the linker molecule could explain the similar currents observed for the Az (with linker) and Apo-Az systems.

Temperature Dependence of the Conductance (dI/dV) Peaks

To discriminate between two possible causes for the conductance peaks, namely resonant tunneling and Coulomb blockade, we measured the temperature dependence of both I-V and (dI/dV)-V for the Au-Az/linker-Au junctions. Temperature-dependent measurements were carried out using both MPA (presented in Fig. 5) and MHA (*SI Appendix*) linkers, which differ in length.

Fig. 5 *A–C* shows the I-V and the dI/dV determined for Au-Az/MPA-Au junctions at different temperatures. On increasing the temperature, the steps in the I-Vs are progressively washed out, the conductance peaks are broadened, and their heights decrease. Fig. 5*D* shows all of the conductance peaks observed at different temperatures from 10 to 60 K. Fig. 5*E* is a zoomed in view of the conductance peaks at positive bias at varying temperature, showing how the height of the conductance peak decreases and broadens with increasing temperature. Thermal fluctuations can cause small variation in the interaction between the linker and the Cu(II) site, leading to a random shift in the peak position during the conductance measurement at different temperatures as observed in Fig. 5*E*.

At first glance, this temperature dependence resembles that observed in the Coulomb blockade regime in weakly coupled molecular junctions ($\Gamma << k_BT$) (49), where Γ defines the coupling parameter, k_B is Boltzmann constant, and T is temperature. However, closer inspection shows that the broadening of the dI/dV peaks is larger than that caused by the thermal energy k_BT ($\Gamma >> k_BT$). Thus, the temperature dependence observed here rules out Coulomb blockade as a dominant cause for the observed peaks (additional details are in *SI Appendix*). As we show below, the thermal broadening is more likely to be the result of the temperature dependence of the Fermi electronic occupational distribution in the leads (50).

Theoretical Modeling

To examine the notion that the redox active orbital of the Cu(II) ion in Az is responsible for the observed current steps, we modeled the I-V behavior of the junction by a single-level model that is widely used in the context of molecular electronics (29, 51, 52) (*SI Appendix* has more details). In this model, transport through a single-molecule junction is assumed to be dominated by elastic tunneling of electrons through a single molecular level of energy ε_0 coupled to the left (L) and right (R) electrodes with a strength $\Gamma_{L,R}$. The I-V relation in this model is obtained by using the Landauer formula with the single-level transmission function, and the temperature dependence is incorporated in the Fermi distribution function of the electrodes. We used this model to reproduce the observed temperature dependence of individual conductance peaks in our experimental results. In Fig. 6*A*, we show an example of the temperature dependence of the differential conductance predicted by this model. In this case, the total broadening is $\Gamma = 10$ meV (k_BT at 10 K is ~0.9 meV), ε_0 was chosen to reproduce the experimental peak position, and we assumed a very asymmetric situation $\Gamma_L >> \Gamma_R$ to mimic our protein junctions, which are bound covalently via an Au-S bond to only one of the electrodes. As one can see, the results nicely reproduce the observed bias and temperature dependence of the differential conductance patterns (Fig. 5*E*). It is noteworthy that this model is meant to describe a single-molecule junction. Hence, one has to be cautious with the values of the tunneling rates used here (Fig. 6*A*). However, it is very encouraging to see that this simple model can even reproduce the order of magnitude of the dI/dV. This suggests that the observed individual conductance peaks are related to the transport through a single or a few protein molecules. Overall, these results strongly support the idea that the observed step-like I-Vs patterns are a signature of resonant tunneling through discrete electronic levels (Fig. 6*D*). This single-level model can also reproduce the features of the off-resonance tunneling via the junction without linker molecule (Fig. 6*C*), such as their I-V shape and temperature dependence (detailed in *SI Appendix*). Thus, it may be considered to function as a unified theory.

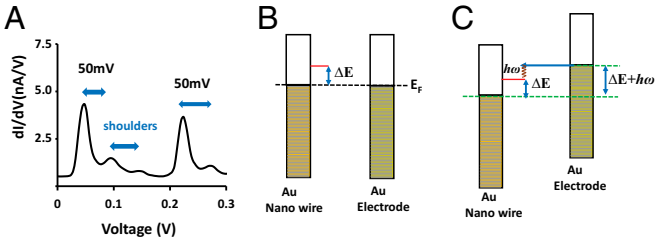

Fig. 7. (*A*) Conductance–voltage plot of the Az junction with MPA linker between 0 and +0.5 V showing the presence of the satellite peak ~50 mV away from the main peak. *B* shows the scheme of electronic energy levels without any applied bias (for simplicity, just one energy level is shown). *C* shows the scheme of the vibrational modes of the resonant electronic state due to vibronic interaction.

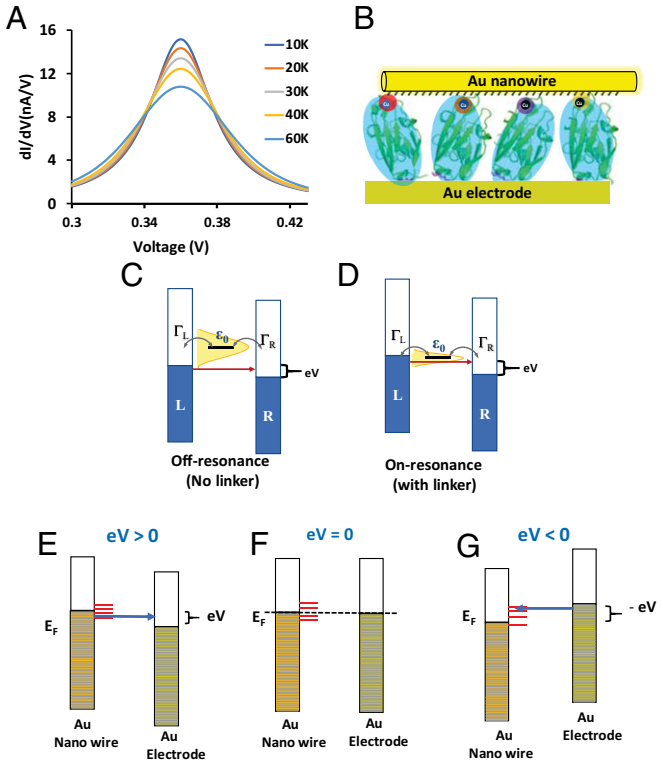

Fig. 6. (*A*) Differential conductance as a function of the bias voltage computed with the resonant tunneling model with $\varepsilon_o = 0.18$ meV, $\Gamma_L = 10$ meV, and $\Gamma_R = 1$ μeV. The different curves correspond to the different indicated temperatures. (*B*) Schematic illustration of a solid-state protein junction with slightly different orientations of the Az (and the Cu coordination sphere) with respect to the linker molecules closest to it. *C* shows schematically the off-resonant tunneling case in the absence of the linker at an applied bias, V. The strong coupling is expressed by the large broadening of the energy levels (shown in yellow Lorentzian); ε_o represents the energetic alignment of the Cu(II) localized electronic states with respect to the Au Fermi level (E_F), and Γ_R and Γ_L denote the coupling strength of the protein to the right and left electrodes, respectively. In the strong coupling case, the electron tunneling takes place through the tail of the molecular resonance, and the smooth energy dependence of the transmission in the transport window makes the I-V curves linear. *D* shows an on-resonant tunneling case in the presence of the linker at an applied bias, V. The Cu(II) localized electronic states (horizontal black bars) for the on-resonant case fall within the applied bias window, V. *E*–*G* show schematics of possible electronic energy-level shifts of the entire junction (on resonance case) with applied bias. *E* presents the case where a small bias (+V) is applied across the junction. *F* shows the scheme of electronic energy levels before any applied bias. *G* shows the energy levels of entire junctions across a small negative bias (–V).

An obvious question arises from our above analysis regarding the origin of the multiple peaks that we observe in the conductance spectra. These generally indicate multiple electronic states accessible for resonance in the Az junction with linkers. The Cu(II) center of Az has only one redox active molecular orbital energy level [i.e., the molecular orbitals formed on hybridization of the Cu(II) $3dx^2$-y^2 orbital and the S p orbital of Cys-84, which is close in energy to the work function of the Au electrode and is accessible in our bias window] (53). At the same time, the spacing that we observe experimentally between peaks is far too small to correspond to other electronic energy levels of Cu(II). Therefore, it is not obvious why we see several conductance peaks. Our hypothesis is that the different conductance peaks originate from varied energy levels of the Cu(II) sites due to its different coordination environment. It is well-known that the electronic structure and the available active electronic states of the Cu(II) ion can vary depending on the nature of the metal ion ligands and their geometric configuration (53–55). In our junction, the Cu(II) coordination sphere exposed to the surface of Az and contacting the Au nanowire electrode interacts differently with the linkers that are covalently attached to the Au nanowire. These interactions, in turn, change the energy levels of the Cu(II) coordination sphere for the given linker-Az system ([i.e., slight differences in orientations (Fig. 6*B*) of the Az (and the Cu coordination sphere) with respect to the linker molecules closest to it will result in an ensemble of relatively closely spaced frontier energy levels in the junctions]. Because practically, it is likely that most of the current flows through only a few of the proteins

CHEMISTRY

(42), we get, at low enough temperatures, distinct peaks. This scenario explains the observation of multiple peaks in our junctions with slight variations in their position from junction to junction. Fig. 6 *E–G* expresses this view schematically, illustrating the situation when a bias is applied to the bottom Au electrode, spans a range of energy levels (horizontal red bars in Fig. 6 *E–G*), and gives rise to multiple peaks in the conductance measurements within the applied bias range (±0.5 eV) (Figs. 2 and 3). It is also important to mention that the multiple satellite peaks at the tail of the main resonance peaks in dI/dV seem to be replicas of each other (Fig. 2*C*, black curve), which hint at the possibility that several proteins with slightly different configurations with respect to the electrodes contribute to the conductance (see below).

Vibronic States of Copper Active Site

We further consider the vibronic states of the Cu(II) center to be due to the interaction between the electron and vibrational motion in the Cu(II) coordination sphere. The vibronic states in the conductance spectrum of a junction should be present as progression peaks in the dI/dV–V plot (56). The randomly distributed resonance peaks can, therefore, be easily ruled out as vibronic states. However, the shoulder peaks at the tail of the main resonance peaks that we observed reproducibly in the Au-Az/MPA-Au junction (Figs. 2*C* and 3) do indeed fit the progression pattern of vibronic states. We note that, even when the position of the main peak is shifted in terms of bias in different junctions, the satellite peaks were always positioned at ∼50 mV above the main peak (Fig. 7*A*). Such satellite peak fits a well-known resonant IETS vibrational signal (29), and its origin can be understood as follows. At sufficiently high bias, some of the electrons tunnel inelastically by exciting a vibrational mode of the protein, and after losing part of their energy, they proceed resonantly through Cu(II) center (Fig. 7 *A* and *C*). This explains the appearance of a satellite conductance peak next to the main elastic peak. The difference between main and satellite peaks corresponds to the energy of the vibrational mode associated with the resonant state, similar to the significance of resonant Raman spectroscopy (29, 56). We assign the satellite peak to the Cu-S stretch, specifically the motion of the cysteine sulfur atom (57), which is one of the Cu(II) ligands. All reported dominant Cu-S stretching vibrations, ν (Cu-S), fall around 400 cm^{-1}, consistent with the 50-meV spacing that we observed (58–60). Therefore, these satellite peaks provide direct evidence for the involvement of Cu(II) with its coordination sphere in the resonant state in tunneling charge transport in a working Az molecular junction. Moreover, the fact that the satellite peaks always appear at approximately the same energy difference from the main peaks in a given conductance spectrum (Fig. 7*A*) supports our idea that the conductance peaks actually originate from the transport through distinct proteins.

Conclusions

Our results provide experimental evidence that ETp through Az can be fully coherent. The results obtained by altering the Az–electrode interaction, namely modulating the interaction with one of the electrodes, are consistent with resonant tunneling across Az (i.e., coherent ETp). The vibrational signature of the Cu(II) coordination site provides direct evidence for the role of the Cu(II) site in charge transport across Az. The approach of modifying protein–electrode coupling to study transport mechanism(s) and protein junction characteristics presents a general strategy for investigating protein electronics. As an experimental approach, it can be extended to any redox active or even redox inactive biomolecule.

ACKNOWLEDGMENTS. We thank Prof. Spiros Skourtis (University of Cyprus), Dr. Cunlan Guo, and Mr. Ben Kayser (Weizmann Institute of Science) for fruitful discussions. J.A.F. thanks the Azrieli Foundation for the award of an Azrieli Fellowship. M.S. and D.C. thank the Israel Science Foundation, the Minerva Foundation, the Nancy and Stephen Grand Center for Sensors and Security, the Benoziyo Endowment Fund for the Advancement of Science, and J & R Center for Scientific Research for partial support. M.S. holds the Katzir–Makineni Chair in Chemistry; D.C. held the Schaefer Professorial Chair in Energy Research. J.C.C. acknowledges funding from the Spanish Ministry of Economy, Industry, and Competitiveness (Projects FIS2014-53488-P and FIS2017-84057-P) and thanks the German Research Foundation (DFG) and Collaborative Research Center (SFB) 767 for sponsoring his stay at the University of Konstanz as a Mercator Fellow.

1. Winkler JR, Gray HB, Prytkova TR, Kurnikov IV, Beratan DN (2005) Electron transfer through proteins. *Bioelectronics: From Theory to Applications* (Wiley-VCH, Weinheim, Germany), pp 15–33.
2. Gray HB, Winkler JR (2009) Electron flow through proteins. *Chem Phys Lett* 483:1–9.
3. Ron I, Pecht I, Sheves M, Cahen D (2010) Proteins as solid-state electronic conductors. *Acc Chem Res* 43:945–953.
4. Amdursky N, et al. (2014) Electronic transport via proteins. *Adv Mater* 26:7142–7161.
5. Kumar KS, Pasula RR, Lim S, Nijhuis CA (2016) Long-range tunneling processes across ferritin-based junctions. *Adv Mater* 28:1824–1830.
6. Castañeda Ocampo OE, et al. (2015) Mechanism of orientation-dependent asymmetric charge transport in tunneling junctions comprising photosystem I. *J Am Chem Soc* 137:8419–8427.
7. Alessandrini A, Facci P (2016) Electron transfer in nanobiodevices. *Eur Polym J* 83: 450–466.
8. Baldacchini C, Bizzarri AR, Cannistraro S (2016) Electron transfer, conduction and biorecognition properties of the redox metalloprotein azurin assembled onto inorganic substrates. *Eur Polym J* 83:407–427.
9. Friis EP, Andersen JET, Madsen LL, Moller P, Ulstrup J (1997) In situ STM and AFM of the copper protein Pseudomonas aeruginosa azurin. *J Electroanal Chem* 431:35–38.
10. Zhao J, Davis JJ, Sansom MSP, Hung A (2004) Exploring the electronic and mechanical properties of protein using conducting atomic force microscopy. *J Am Chem Soc* 126: 5601–5609.
11. Li W, et al. (2012) Temperature and force dependence of nanoscale electron transport via the Cu protein azurin. *ACS Nano* 6:10816–10824.
12. Sepunaru L, Pecht I, Sheves M, Cahen D (2011) Solid-state electron transport across azurin: From a temperature-independent to a temperature-activated mechanism. *J Am Chem Soc* 133:2421–2423.
13. Ron I, et al. (2010) Proteins as electronic materials: Electron transport through solid-state protein monolayer junctions. *J Am Chem Soc* 132:4131–4140.
14. Amdursky N, et al. (2015) Electron transfer proteins as electronic conductors: Significance of the metal and its binding site in the blue Cu protein, azurin. *Adv Sci (Weinh)* 2:1400026.
15. Mukhopadhyay S, Dutta S, Pecht I, Sheves M, Cahen D (2015) Conjugated cofactor enables efficient temperature-independent electronic transport across ∼6 nm long halorhodopsin. *J Am Chem Soc* 137:11226–11229.
16. Amdursky N, et al. (2014) Solid-state electron transport via cytochrome c depends on electronic coupling to electrodes and across the protein. *Proc Natl Acad Sci USA* 111: 5556–5561.
17. Raichlin S, Pecht I, Sheves M, Cahen D (2015) Protein electronic conductors: Hemin-substrate bonding dictates transport mechanism and efficiency across myoglobin. *Angew Chem Int Ed Engl* 54:12379–12383.
18. Yu X, et al. (2015) Insights into solid-state electron transport through proteins from inelastic tunneling spectroscopy: The case of azurin. *ACS Nano* 9:9955–9963.
19. Amdursky N, Pecht I, Sheves M, Cahen D (2013) Electron transport via cytochrome c on Si-H surfaces: Roles of Fe and heme. *J Am Chem Soc* 135:6300–6306.
20. Venkat AS, Corni S, Di Felice R (2007) Electronic coupling between azurin and gold at different protein/substrate orientations. *Small* 3:1431–1437.
21. Frisenda R, van der Zant HSJ (2016) Transition from strong to weak electronic coupling in a single-molecule junction. *Phys Rev Lett* 117:126804.
22. Noy G, Ophir A, Selzer Y (2010) Response of molecular junctions to surface plasmon polaritons. *Angew Chem Int Ed Engl* 49:5734–5736.
23. Galperin M, Ratner MA, Nitzan A, Troisi A (2008) Nuclear coupling and polarization in molecular transport junctions: Beyond tunneling to function. *Science* 319:1056–1060.
24. Smith PA, et al. (2000) Electric-field assisted assembly and alignment of metallic nanowires. *Appl Phys Lett* 77:1399–1401.
25. Freer EM, Grachev O, Duan X, Martin S, Stumbo DP (2010) High-yield self-limiting single-nanowire assembly with dielectrophoresis. *Nat Nanotechnol* 5:525–530, and erratum (2010) 5:625.
26. Sepunaru L, et al. (2015) Electronic transport via homopeptides: The role of side chains and secondary structure. *J Am Chem Soc* 137:9617–9626.
27. Troisi A, et al. (2007) Tracing electronic pathways in molecules by using inelastic tunneling spectroscopy. *Proc Natl Acad Sci USA* 104:14255–14259.
28. Danilov A, et al. (2008) Electronic transport in single molecule junctions: Control of the molecule-electrode coupling through intramolecular tunneling barriers. *Nano Lett* 8:1–5.

29. Cuevas JC, Scheer E (2017) *Molecular Electronics: An Introduction to Theory and Experiment* (World Scientific, Singapore).
30. Su TA, Neupane M, Steigerwald ML, Venkataraman L, Nuckolls C (2016) Chemical principles of single-molecule electronics. *Nat Rev Mater* 1:16002.
31. Moth-Poulsen K, Bjørnholm T (2009) Molecular electronics with single molecules in solid-state devices. *Nat Nanotechnol* 4:551–556.
32. Sayed SY, Fereiro JA, Yan H, McCreery RL, Bergren AJ (2012) Charge transport in molecular electronic junctions: Compression of the molecular tunnel barrier in the strong coupling regime. *Proc Natl Acad Sci USA* 109:11498–11503.
33. Selzer Y, Allara DL (2006) Single-molecule electrical junctions. *Annu Rev Phys Chem* 57:593–623.
34. Nitzan A, Ratner MA (2003) Electron transport in molecular wire junctions. *Science* 300:1384–1389.
35. Perrin ML, et al. (2013) Large tunable image-charge effects in single-molecule junctions. *Nat Nanotechnol* 8:282–287.
36. Skov LK, Pascher T, Winkler JR, Gray HB (1998) Rates of intramolecular electron transfer in Ru(bpy)(2)(im)(His83)-modified azurin increase below 220 K. *J Am Chem Soc* 120:1102–1103.
37. Tian WD, et al. (1998) Conductance spectra of molecular wires. *J Chem Phys* 109:2874–2882.
38. Datta S, et al. (1997) Current-voltage characteristics of self-assembled monolayers by scanning tunneling microscopy. *Phys Rev Lett* 79:2530–2533.
39. Porath D, Levi Y, Tarabiah M, Millo O (1997) Tunneling spectroscopy of isolated C-60 molecules in the presence of charging effects. *Phys Rev B* 56:9829–9833.
40. Hayakawa R, Hiroshiba N, Chikyow T, Wakayama Y (2011) Single-electron tunneling through molecular quantum dots in a metal-insulator-semiconductor structure. *Adv Funct Mater* 21:2933–2937.
41. Vilan A, Aswal D, Cahen D (2017) Large-area, ensemble molecular electronics: Motivation and challenges. *Chem Rev* 117:4248–4286.
42. Du W, et al. (2016) On-chip molecular electronic plasmon sources based on self-assembled monolayer tunnel junctions. *Nat Photonics* 10:274–280.
43. Nitzan A (2001) A relationship between electron-transfer rates and molecular conduction. *J Phys Chem A* 105:2677–2679.
44. Nitzan A (2002) The relationship between electron transfer rate and molecular conduction. 2. The sequential hopping case. *Isr J Chem* 42:163–166.
45. Traub MC, Brunschwig BS, Lewis NS (2007) Relationships between nonadiabatic bridged intramolecular, electrochemical, and electrical electron-transfer processes. *J Phys Chem B* 111:6676–6683.
46. Berlin YA, Ratner MA (2005) Intra-molecular electron transfer and electric conductance via sequential hopping: Unified theoretical description. *Radiat Phys Chem* 74:124–131.
47. Venkatramani R, Wierzbinski E, Waldeck DH, Beratan DN (2014) Breaking the simple proportionality between molecular conductances and charge transfer rates. *Faraday Discuss* 174:57–78.
48. Wierzbinski E, et al. (2013) The single-molecule conductance and electrochemical electron-transfer rate are related by a power law. *ACS Nano* 7:5391–5401.
49. Thijssen JM, Van der Zant HSJ (2008) Charge transport and single-electron effects in nanoscale systems. *Phys Status Solidi B* 245:1455–1470.
50. Garrigues AR, Wang L, Del Barco E, Nijhuis CA (2016) Electrostatic control over temperature-dependent tunnelling across a single-molecule junction. *Nat Commun* 7: 11595.
51. Poot M, et al. (2006) Temperature dependence of three-terminal molecular junctions with sulfur end-functionalized tercyclohexylidenes. *Nano Lett* 6:1031–1035.
52. Zotti LA, et al. (2010) Revealing the role of anchoring groups in the electrical conduction through single-molecule junctions. *Small* 6:1529–1535.
53. Solomon EI, et al. (2014) Copper active sites in biology. *Chem Rev* 114:3659–3853.
54. Winkler JR, Gray HB (2014) Electron flow through metalloproteins. *Chem Rev* 114: 3369–3380.
55. Ambundo EA, et al. (1999) Influence of coordination geometry upon copper(II/I) redox potentials. Physical parameters for twelve copper tripodal ligand complexes. *Inorg Chem* 38:4233–4242.
56. Galperin M, Ratner MA, Nitzan A (2007) Molecular transport junctions: Vibrational effects. *J Phys Condens Matter* 19:103201.
57. Thamann TJ, Frank P, Willis LJ, Loehr TM (1982) Normal coordinate analysis of the copper center of azurin and the assignment of its resonance Raman spectrum. *Proc Natl Acad Sci USA* 79:6396–6400.
58. Andrew CR, et al. (1994) Raman-spectroscopy as an indicator of cu-s bond-length in type-1 and type-2 copper cysteinate proteins. *J Am Chem Soc* 116:11489–11498.
59. Andrew CR, Loehr TM, Sandersloehr J (1994) Raman-spectroscopy as an indicator of cu-s bond lengths and coordination geometries in copper-cysteinate proteins. *J Am Chem Soc* 208:362.
60. Dave BC, Germanas JP, Czernuszewicz RS (1993) The 1st direct evidence for copper(II) cysteine vibrations in blue copper proteins–Resonance Raman-spectra of s-34-cys-labeled azurins reveal correlation of copper sulfur stretching frequency with metal site geometry. *J Am Chem Soc* 115:12175–12176.